ICSV14
Cairns • Australia
9-12 July, 2007

USE OF SCATTERING OF ULTRASOUND PULSES AND SHOCK WAVES BY KIDNEY STONES FOR IMAGING IN LITHOTRIPSY

Oleg A. Sapozhnikov[1, 2], Neil R. Owen[2], Michael R. Bailey[2], Alexander I. Gromov[3], and Lawrence A. Crum[2]

[1]Department of Acoustics, Physics Faculty, Moscow State University,
Leninskie Gory, Moscow 119992, Russia
[2]Center for Industrial and Medical Ultrasound, Applied Physics Laboratory,
University of Washington, 1013 NE 40th Street, Seattle WA 98105, USA
[3]Mandryka 2nd Central Clinical Military Hospital, 8A Bolshaya Olenya Street,
Moscow 107014, Russia
olegs@apl.washington.edu

Abstract

Shock wave lithotripsy, as a procedure for kidney stones fragmentation, would be more efficient if the kidney stone position and size are estimated, and if the progress of the stone fragmentation by shock waves is assessed. These two challenges can be addressed using scattering of ultrasound waves on stones. Although the acoustic impedance of stones often differs by more than a factor of 2 from surrounding tissue, stones are not always readily visible on B-mode ultrasound, for example because a small stone can be lost in the speckle of the kidney tissue. However, we and others have found stones can be made to light up on Doppler imaging in what is called a “twinkling artifact”, that may be in part due to stone displacement by acoustic radiation force and partly due to multiple scattering at rough edges. As for fragmentation feedback, fractures in the stone push the frequency of resonance scattering of lithotripter shock wave to bands related to the reverberation period of the pieces. Acoustic scattering of the diagnostic pulses and shock waves by the stones was calculated numerically using a linear elastic model, initialized with known elastic constants. Based on this data, acoustic radiation force and scattered field in the farfield were calculated using integral representation of the corresponding parameters. These methods provide new ways to locate kidney stone stones and to monitor the fragmentation process.

1. INTRODUCTION

One of remarkable applications of nonlinear acoustic waves is extracorporeal shock wave lithotripsy (SWL), which is a method to comminute kidney stones by focused shock waves. During SWL, several thousand acoustic shock waves are generated outside the body and used to break a stone into fragments that are small enough to pass from the urinary tract. Today, SWL is the preferred method to treat kidney stones. However, recent work indicates that tissue injury accompanies most if not all SWL treatments [1], which can lead to acute and chronic complications [2].

Stone targeting and the assessment of fragmentation are two ways that lithotripsy could be improved, but there is currently little feedback available to determine if a SW hits the stone or if the stone is breaking. Fluoroscopy imaging and B-mode ultrasound imaging are two modalities used during SWL. [3] Though helpful for targeting, use of fluoroscopy is limited by the associated radiation dose. Also based on fluoroscopy images it is difficult to discern whether the stone is breaking. Fluoroscopy images and ultrasound B-images do not clearly indicate fragmentation. Presented in this paper and tested *in vitro* is a new method to identify stone fragmentation. To do it, we developed a frequency analysis method to detect changes in SW scattering associated with the stone breaking into smaller pieces. The output of that method could aid a urologist in deciding whether to continue or stop SWL. If a stone were not breaking, the urologist could stop SWL and avoid excessive SW dose. The motivation for this work was to improve SWL by maximizing fragmentation for a given number of SWs and by identifying fragmentation. Stones with little chance of breaking might be screened from SWL treatment.

B-mode ultrasound imaging is real-time and can be used continuously during SWL, but small stones are difficult to distinguish from other tissue. Additional information during ultrasound imaging can be gained in Doppler mode that is aimed in measuring tissue movement, usually blood flow. In clinical practice, color Doppler artifacts are routinely encountered [4]. Color is not always an indication of blood flow. Rahmouni *et al*. [5] first described so called “twinkling artifact” that appears behind calcifications in various tissues, in particular, behind urinary stones. The twinkling artifact usually is seen as a random color encoding, i.e. a rapidly changing mixture of red and blue, behind the stones in the region where shadowing would be expected on B-mode (gray scale) images; however, sometimes the color is present only at the stone image [6]. The artifact can also be seen by power Doppler sonography [5, 7]. Because the twinkling artifact may be considered an additional sonographic feature of urinary stones, it may be helpful in ultrasound determining the presence of the stones. Present knowledge of mechanisms that cause the twinkling artifact is limited. Acoustic interference due to reflection from rough stone surface, resonant scattering, and intrinsic noise of the ultrasound machine have been proposed as possible reasons for the effect [8, 9]. Little is done to study the physics of the phenomena involved in Doppler pulse interaction with stones. Here we report on investigation of a possible mechanism that may be important for small stones, namely true movement of the stones due to radiation pressure.

2. RESONANT SCATTERING OF SHOCK WAVES BY KIDNEY STONES

2.1 Theoretical background for resonant scattering

In previous work with model stones made of glass, the frequency of resonant acoustic scatter was related to the period of one reverberation in the stone model [10]. Therefore, a simple estimator for the frequency of reverberation for a given sound speed and stone size is

$$f = \frac{c}{2d}, \tag{1}$$

where f is frequency, c is sound speed of the stone model, and d is diameter. Using a sound speed of 2.7 mm/μs, stones of 2 mm diameter or smaller reverberate at a frequency of 675 kHz or higher.

2.2 Methods and Materials

To measure acoustic scatter at various stages of stone fragmentation, model stones made of cement were held in a low-density polyethylene (LDPE) pipette, placed individually at the focus of an electrohydraulic research lithotripter [11], and subjected to 30 shock waves (SWs). The cement stones had 5 mm radius, 2.7 mm/μs sound speed, 1.15 g/cm^3 density, and were fragile to SWs. Figure 1 shows the experimental arrangement. A passive, spherically focused receiver was positioned confocally with the lithotripter to detect and measure SW scattering from the stone models. It had 150 mm focal distance for remote detection from outside the aperture of the SW source. The lithotripter SW and data collection with the oscilloscope were triggered by the waveform generator at a rate of 1 SW/min or slower, which allowed bubbles to dissolve between SWs [12]. Scatter signals were high pass filtered at 100 kHz (3202, Krohn-Hite Corp., www.krohn-hite.com), digitized at a sampling rate of 50 MS/s (TDS744A, Tektronix Inc., www.tek.com), transferred to a computer over GPIB using LabVIEW (National Instruments Corp., www.ni.com) software, and saved to memory. Each SW was generated with a lithotripter charging potential of 18 kV and water was degassed to less than 10% of saturation.

The use of subtraction to remove background effects is common in scattering experiments. The pipettes were made of LDPE, which has 0.92 g/cm^3 density and 2.06 mm/μs sound speed. The characteristic acoustic impedance was 1.9 Mrayls, 27% higher than the characteristic acoustic impedance of water and may have affected the data [13]. Scatter from the pipette without a stone inside was measured from 20 SWs triggered at 1 SW/min using a charging potential of 18 kV.

High-speed photographs were taken concurrently with scatter measurements to visualize stone fragmentation and cavitation. A high-speed camera (Imacon 200, DRS Technologies, www.drsdigitalimaging.com) with 105 mm lens and 27.5 mm extender captured a field of view that was 2.0 cm x 2.4 cm in 980 x 1200 pixels, and perpendicular to the axes of both the SW and the spherically focused receiver (through the page in Fig. 1). A 1000 W flash bulb was placed beside the camera to illuminate the field. For each of the 30 SWs triggered, a photograph was taken at 26 μs after arrival of the SW at the pipette surface.

Scatter signals measured with the broadband receiver were processed in time and

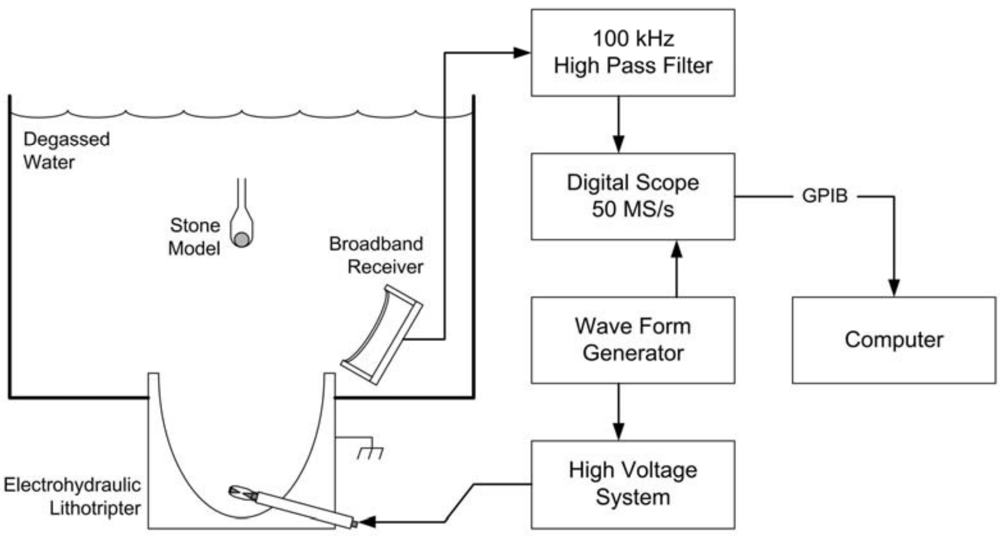

Figure 1. Arrangement of the lithotripter, stone model, and equipment used to measure SW scattering from stone models.

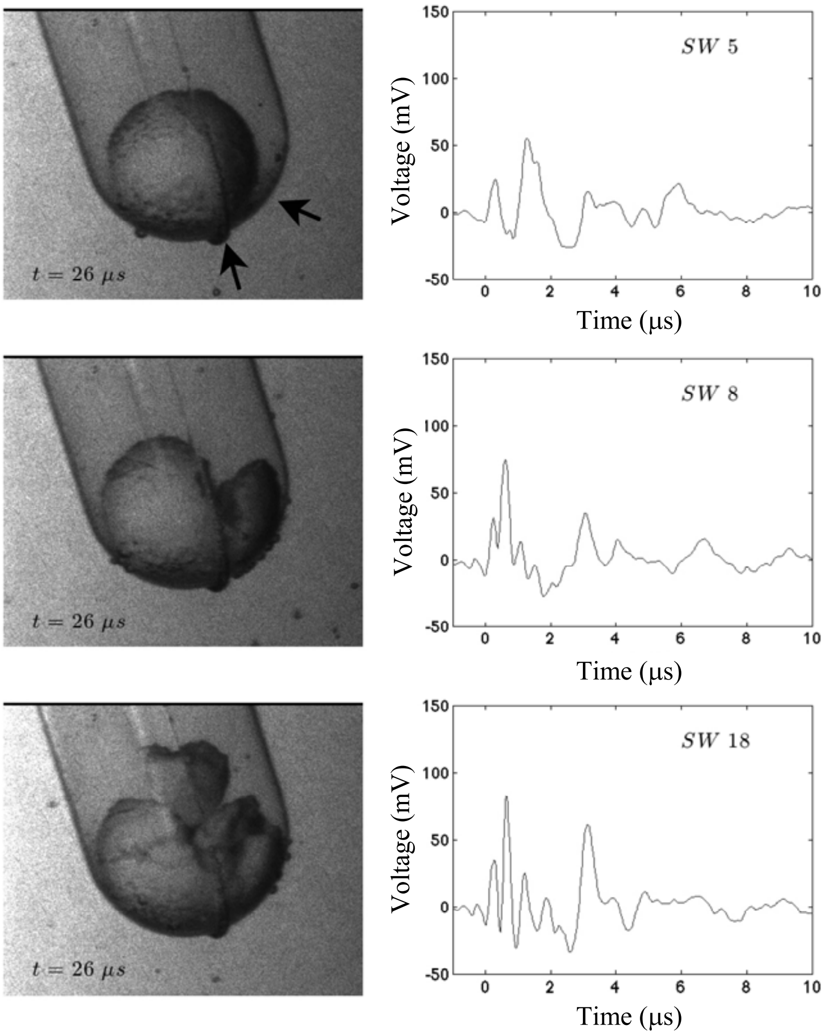

Figure 2. High speed photographs and measured scatter from SWs 5, 8, and 18. Photographs and the corresponding scatter signal are columnated in pairs. Arrows show the axes of the SW (bottom) and the receiver (right).

frequency. Time domain processing included three steps. First, each signal, including those measured from the pipette only, was low pass filtered at 5 MHz with an equiripple FIR filter. Second, each signal was deconvolved remove effects of the 100 kHz high pass filter used during measurement. Last, each signal was manually aligned to have t=0 coincide with arrival of the SW at the pipette surface. Temporal realignment was necessary to correct for jitter in SW triggering. Frequency domain processing included several steps. First, an average of the 20 signals measured from the pipette was subtracted from each time domain signal. Second, a 5 μs segment starting at t=0 μs was retained and all other segments of the signal were discarded. Third, the power spectrum of each signal was calculated. Fourth, each power spectrum was normalized to unit energy by enforcing the condition

$$\sum_{k=0}^{N-1} W_k \Delta f = 1, \tag{2}$$

where W_k is the power spectrum, Δf is the difference between adjacent samples in frequency, N is the length of the signal, and k is an index variable. Fifth, mean spectra were calculated for scatter measured from SWs 1 to 5, and for scatter measured from SWs 26 to 30. In the last step, a ratio was calculated to display the redistribution of spectral energy to higher frequencies. The mean spectrum from the last five SWs was divided by the mean spectrum of the first five SWs,

$$R_k = \frac{\overline{W}_{L,k}}{\overline{W}_{F,k}}, \tag{3}$$

where R_k is the ratio of energy, $\overline{W}_{L,k}$ is the mean spectrum for the last five SWs, is the mean spectrum for the first five SWs, and k is an index variable for frequency.

2.3 Results

Figure 2 shows high-speed photographs and the corresponding scatter signals measured from SWs 5, 8, and 18. After 5 SWs, the stone was intact and the scatter signal was representative of the previous 4 measurements. The spike between 0 μs and 0.5 μs was the reflection of the SW off the pipette surface. Reflection of the SW off the stone was from 1 μs to 3 μs, followed by reverberations of the SW within the stone. The gap between reflections off the pipette and stone corresponds to the propagation distance between them along the receiver axis. Further, the characteristic acoustic impedance of the stone was 3.1 Mrayls, 63% higher than that of the pipette; the reflection from the stone surface had higher amplitude. After 8 SWs, the stone was fragmented and characteristics of the scatter signal changed accordingly. The gap between the pipette and stone shortened, and the remainder of the signal was a combination of reflections and reverberations from the fragments. Similar changes occurred in the signal measured from SW 18, where fragmentation was visibly increased. Note, the photographs were taken at 26 μs after arrival of the SW at the pipette surface to allow bubbles to grow to a visible size. Measured scatter signals ended at 10 μs.

Figure 3 shows the mean power spectra for the first and last 5 SWs, and the ratio of the mean power spectra calculated with Eq.(3). Compared to the mean power spectrum for the first 5 SWs, the mean power spectrum for the last 5 SWs had lower amplitude from 0.1 MHz to 0.7 MHz and higher amplitude from 0.7 MHz to 1.2 MHz. Energy was redistributed to higher frequencies as stone fragmentation increased. The ratio of spectra is a simpler display of the same information. Ratio values less than 1 indicate a decrease in energy and values greater than 1 indicate an increase in energy. Energy in the frequency range from 0.7 MHz to 1.2 MHz increased with stone fragmentation and peaked at 0.88 MHz. Using Eq.(1), ratio values above 1 in Fig. 3 accord with stone fragments smaller than 2 mm.

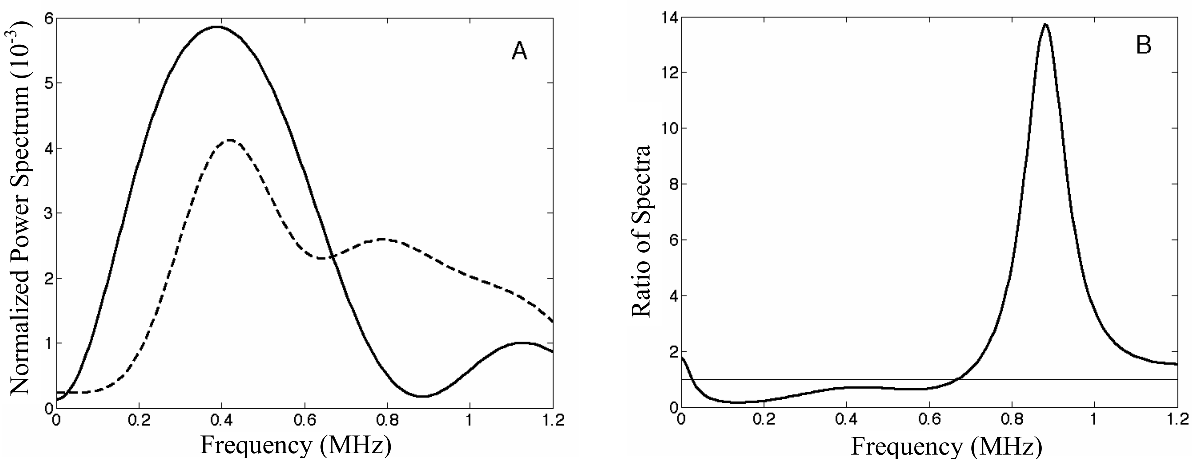

Figure 3. (A) Mean power spectrum for the first 5 SWs (solid line) and mean power spectrum for the last 5 SWs (dashed line). (B) Ratio of spectra calculated with Eq. (3). The solid line at a ratio value of 1 was added to represent the ratio of identical spectra.

3. RADIATION FORCE AS A REASON FOR TWINKLING ARTICACT IN COLOR DOPPLER IMAGING OF SMALL KIDNEY STONES

3.1 Theoretical background for radiation force

Typical occurrence of the twinkling artifact is shown in Fig.3, where the image of kidney with a stone is presented. The question arises: is it truly artifact, or perhaps stone is actually moving?

A possible movement for the stone is radiation force that appears when the Doppler pulse is scattered at it. The acoustic radiation force is usually defined as a time-average force exerted on the scatterer by a sound wave. A well-known example of its usage is measurement of total power of ultrasonic sources. The radiation force is associated with the acoustic radiation force tensor T_{ij}, whose elements are given by:

$$T_{ij} = -\left(\frac{p^2}{2\rho_0 c_0^2} - \frac{\rho_0 \mathbf{u}\cdot\mathbf{u}}{2} \right)\delta_{ij} - \rho_0 u_i u_j \tag{4}$$

Here p is acoustic pressure, $\mathbf{u} = (u_1, u_2, u_3)$ is particle velocity, ρ_0 and c_0 are medium density and seed of sound, and δ_{ij} is the Kroneker delta. Radiation force acting on a volume inside a closed surface Σ has the following components:

$$F_i = -\oiint_{\Sigma} T_{ij} n_j ds\,, \tag{5}$$

where $\mathbf{n} = (n_1, n_2, n_3)$ is inner normal unit vector. Therefore, for the known acoustic field the radiation force can be calculated straightforward. Usually more difficult problem is calculating of the scattered at the object acoustic field, because, in general case, its structure is impossible to express analytically and numerical solution has to be used.

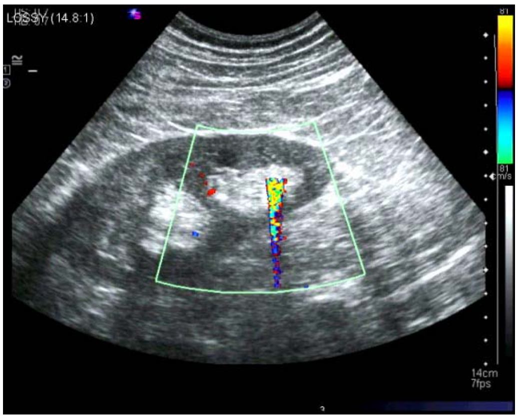

Figure 4. Typical appearance of the twinkling artifact. A colored bright stripe is seen behind a stone in kidney.

3.2 Numerical modeling of the Doppler pulse scattering at a kidney stone

The stone and surrounding liquid are considered as an isotropic medium. The dynamics of such a medium is governed by the equation of motion

$$\rho \frac{\partial v_i}{\partial t} = \frac{\partial \sigma_{ij}}{\partial x_j}\,, \tag{6}$$

where $v_i = \partial u_i / \partial t$ are medium velocity components (u_i are displacement vector components), and σ_{ij} are components of elastic stress tensor. In the linear approximation, that is valid for small strains, elastic forces are governed by Hooke's law:

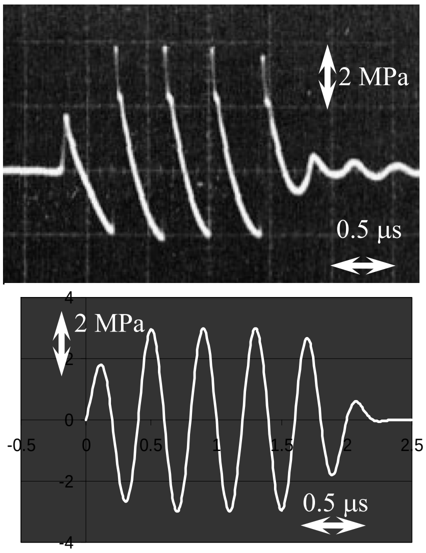

Figure 5. *Top*: Pressure waveform 70 mm from a 2.5 MHz sector array operating in pulsed Doppler mode (adapted from [15]). *Bottom:* Theoretical waveform used in numerical model.

$$\sigma_{ij} = \lambda(\nabla \mathbf{u})\delta_{ij} + \mu\left(\frac{\partial u_i}{\partial x_j} + \frac{\partial u_j}{\partial x_i}\right), \qquad (7)$$

Here λ and μ are Lamé constants (μ is also called shear modulus). We suppose in below that the stone has an axisymmetric shape with the axis oriented along the initial Doppler pulse propagation. The details of the finite difference numerical scheme and used mechanical properties of the stone are presented in [14]. In contrary to [14], where lithotripsy SW scattering was studied, here the incident pressure waveform is taken similar to the experimental Doppler pulse (see Fig.5): $p = p_0 \cdot e^{-r^2/a^2 - (t-\tau)^6/\tau^6} \sin(2\pi f t)$ with appropriately chosen parameters.

The modeling shows how the ultrasound pulse is scattered at the stone, with account of both longitudinal and shear waves inside the stone. For purpose of calculating radiation force, however, only pressure and velocity at some closed surface outside the stone are necessary. A typical pattern of scattered pressure around the stone is shown in Fig.6. Dotted line shows the surface Σ where stress tensor and the corresponding radiation force are calculated from Eqs.(4) and (5), black square shows the stone. Initially, the Doppler pulse incidents on the stone from the left-hand side. At the moment shown in Fig.6 this pulse has partly reflected (left from the stone) and partly scattered in other directions. Due to axial symmetry, the net radiation force has only axial component, F_z. Supposing that the stone is free, the stone velocity increase can be calculated simply as $V = m^{-1}\int F_z dt$, where m is the stone mass. Figure 7 shows calculated velocity for different stone diameters. Note that the velocity increases when the stone becomes smaller. For a 0.5-mm stone, for instance, the velocity is 1 cm/s. This value will be somewhat reduced due to ultrasound pulse absorption in tissue on the way to the stone. But, on the other hand, in Doppler regime the number of pulses used for each color scan line (ensemble length) is 10 to 20 [16], so the net velocity of the stone can reach 10 cm/s, which is large enough to create a significant Doppler shift.

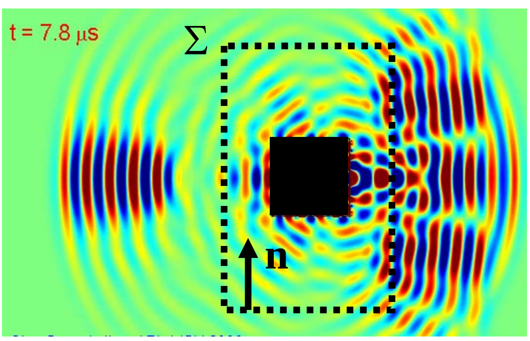

Figure 6. Acoustic pressure distribution during scattering of a Doppler pulse at a cylindrical stone.

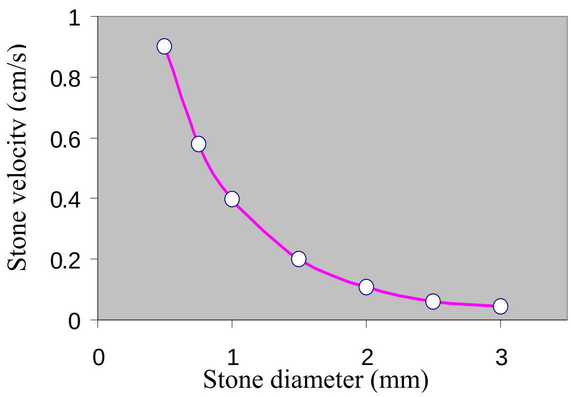

Figure 7. Stone velocity due to scattering of one Doppler pulse, *versus* stone diameter.

4. DISCUSSION AND CONCLUSIONS

SW scattering from model stones made of cement was measured *in vitro* with a broadband receiver. High-speed photographs were taken concurrently with measurement to visualize stone fragmentation and cavitation. Measured scatter signals were processed in the time domain to compare with the photographs, and in the frequency domain to display the redistribution of spectral energy as stone fragmentation increased. Ratio values above 1 in Fig. 3A related to stone fragments smaller than 2 mm.

Figure 2 shows a clear difference in scatter as stone fragmentation increased. The frequency of RAS became visibly higher and the structure of scatter agreed with the size and location of fragments in the pipette. Frequency analysis, shown in Fig. 3, displayed the redistribution of energy with mean power spectra, and with a new method, the ratio of spectra, which was developed to display the redistribution of energy without having to visually inspect two spectra for differences.

The modeling of the radiation force to small kidney stones has demonstrated that the twinkling artifact can be related to the induced motion of the stones.

[Work supported by NIH DK43881, DK55674, NSBRI SMS00402, and RFBR.]

REFERENCES

[1] A.P. Evan, L.R. Willis, J.E. Lingeman, and J.A. McAteer, "Renal trauma and the risk of long-term complications in shock wave lithotripsy", *Nephron* **78**, 1–8 (1998).

[2] J. E. Lingeman and J. R. Newmark, *Kidney Stones: Medical and Surgical Management*. Lippinicott-Raven, Philidelphia, 1996.

[3] P.N. Rao, "Imaging for kidney stones", *World Journal of Urology* **22**(5), 323–327 (2004).

[4] D.G. Mitchell, "Color Doppler imaging: principles, limitations, and artefacts", Radiology **177**, 1-10 (1990).

[5] A. Rahmouni, R. Bargoin, A. Herment, N. Bargoin, and N. Vasile, "Color Doppler twinkling artifact in hyperechoic regions", *Radiology* **199**(1), 269–271 (1996).

[6] A.Y. Vasiliev and A.I. Gromov, "Color doppler mapping with use of power doppler to estimate a pathology of prostate", *Journal of Military Medicine (Voenno-meditsinskii zhurnal)* **318**(4), 33-37 (1997), in Russian.

[7] J.Y. Lee, S.H. Kim, J.Y. Cho, and D. Han, "Color and power Doppler twinkling artifacts from urinary stones: Clinical observations and phantom studies", *American Journal of Roentgenology* **176**(6), 1441–1445 (2001).

[8] A. Kamaya, T. Tuthill, and J.M. Rubin, "Twinkling artifact on color Doppler sonography: Dependence on machine parameters and underlying cause", *American Journal of Roentgenology* **180**(1), 215–222 (2003).

[9] S.P. Weinstein, C. Seghal, E.F. Conant, and J.A. Patton, "Microcalcifications in breast tissue phantoms visualized with acoustic resonance coupled with power Doppler US: initial observations", *Radiology* **224**(1), 265–269 (2002).

[10] N.R. Owen, O.A. Sapozhnikov, M.R. Bailey, L.A. Trusov, and L.A. Crum, "The use of resonant scattering to identify stone fracture in shock wave lithotripsy," *J. Acoust. Soc. Amer.* **121**, EL41-EL47 (2007).

[11] R.O. Cleveland, M.R. Bailey, N.S. Fineburg, B. Hartenbaum, M. Lokhandwalla, J.A. McAteer, and B. Sturtevant, "Design and characterization of a research electrohydraulic lithotripter patterned after the Dornier HM3," *Rev. Sci. Instr*. **6**, 2514-2525 (2000).

[12] T.G. Leighton, *The Acoustic Bubble*, Academic Press, 1994.

[13] R.O. Cleveland, J.A. McAteer, S.P. Andreoli, and L.A. Crum, "The effect of polypropylene vials on lithotripter shock waves," *Ultrasound in Medicine & Biology* **6**, 939-952 (1997).

[14] O.A. Sapozhnikov, A.D. Maxwell, B. MacConaghy, and M.R. Bailey, "A mechanistic analysis of stone fracture in lithotripsy", *J. Acoust. Soc. Amer.* **112**(2), 1190-1202 (2007).

[15] F.A. Duck *et al*., *Clin. Phys. Phisiol. Meas*. **8** (1), 39-49 (1987).

[16] F.W.Kremkau, *Diagnostic Ultrasound: Principles and Instruments*, Philadelphia, 1998